EVOLVING INTERMEDIATE MASS-RATIO INSPIRALS IN THE PRESENCE OF DARK MATTER

Benjamin Wade
Advisor: Dr. David A. Nichols
Department of Physics, University of Virginia

April 3, 2026

Abstract

Massive black holes can grow in the presence of dark-matter environments and form dark-matter spikes with large densities. When a massive black hole within a dark-matter environment is part of an inspiral with a second compact object, the environmental effects will be imprinted on the system's dynamics. Past work studying these systems has demonstrated dynamical friction from the dark-matter distribution can have measurable impacts on the binary inspiral rate. The emitted gravitational waves will be affected in turn; given that they will be in the observable band for upcoming space-based detectors like LISA, the dynamics of dark matter on these scales can be understood precisely. To enhance waveform modeling, we overview a generalization of dynamical friction suitable for spherical systems. Motivated by the observation that the Chandrasekhar formula fails to capture some detailed features of dynamical friction for these systems, we explore and apply the theory of spherical torques. After outlining the derivation of the torque formula, we present strategies to evaluate the torque. With a careful combination of these integration strategies, we present a methodology for determining the torque, including contributions at high multipole order while maintaining computational efficiency.

1 Introduction

Observations of gravitational waves from compact-object mergers serve as one of the most promising avenues for learning about astrophysical systems and have provided a new messenger to complement electromagnetic studies. Here, we focus on mergers of stellar-mass black holes and neutron stars with supermassive black holes in nuclear clusters, which may be observed by upcoming space-based gravitational-wave detectors. The signals from these sources will serve as very sensitive probes of the physical conditions of their environments. As a result, they offer a fantastic opportunity to probe the astrophysical processes in galactic nuclei. Cosmological simulations predict that massive black holes may be surrounded by dense dark-matter halos, suggesting that these environments may alter the dynamics around these black holes. As such, the effects of a dark matter halo may be imprinted on the gravitational-wave signal from inspirals in these systems. Quantifying these effects is important both for proper modeling of the gravitational signal and for extracting useful science about the environment from observations.

Of the potential environmental effects from dark matter, dynamical friction is the primary mechanism through which the compact object loses energy and angular momentum to the collisionless background. This effect can be modeled as a series of cumula-

tive gravitational scatterings of the medium off the massive object under consideration. When the individual components in the distribution (in this case, dark-matter particles) are considerably less massive than the object under consideration (namely, the lighter black hole among the binary), this tends to act as a frictional drag-like effect:[1]

$$M_p \frac{\mathrm{d}v_p}{\mathrm{d}t} = -\frac{4\pi G^2 M_p^2}{v_p^2} \log \Lambda \rho(v < v_p) \quad (1)$$

where M_p is the mass of the perturber, v_p is the velocity of the perturber, and $\rho(v < v_p)$ denotes the density of masses moving more slowly than the perturber. $\log \Lambda$, known as the Coulomb logarithm is a factor dependent on the minimum and maximum impact parameters, which is present to regularize the scattering integral at small and large impact parameters.

Dynamical friction has wide applications in astrophysics and has seen considerable success in reproducing observed orbital decay rates in a wide variety of systems. However, the formalism for dynamical friction was derived assuming uniform, linear motion through an infinite medium, something for which cyclic orbital motion through a finite-sized distribution, as is the case for an inspiral, is a poor approximation. While the naïve application of dynamical friction in orbital-type systems has proven to give surprisingly accurate results when compared against observational data, there are nevertheless situations in which it fails. Notably, the definition of the Coulomb logarithm Λ is derived assuming scatterings within a Newtonian potential assuming a linear medium with scattering interactions, which do not strictly happen in an orbital-type system. This introduces theoretical uncertainty into its application for these systems. A more physically-grounded description of dynamical friction in spherical systems is essential for robust modeling of the environmental effects.

Weinberg[7] presented a formalism suitable for computing the equivalent of dynamical friction in spherical systems. In this framework, dynamical friction arises from resonant exchanges of angular momentum between the perturber and the background distribution. This approach provides a physically motivated interpretation of the effective Coulomb logarithm in terms of the system's resonance structure. As such, it provides a more accurate and self-consistent description of dynamical friction applicable for these systems.

In this report, we develop the formalism for spherical torques and apply it to the case of binary black holes embedded in a dark-matter halo. This refined treatment can contribute to improving models of dynamical friction in the case of compact-object inspirals.

2 Derivation of the Torques

In this section, we overview how we arrive at the formula for spherical torques. We largely follow the work of Kaur[5] to arrive at the general form of the torques, which is applicable for an arbitrary potential. We then specialize to the binary compact-object system of interest.

We take the dark matter halo to be described by a (time-dependent) six-dimensional distribution function in position-velocity phase space $f(x, v, t)$, and the potential under which the distribution function evolves by Φ^{tot}. This potential is comprised of the self-consistent potential of the unperturbed, spherically-symmetric background, Φ_0, as well as that from an external force (namely, the gravitational action of the secondary compact object), which we denote Φ_{ext} (and which will be the relevant potential for the calculation of the

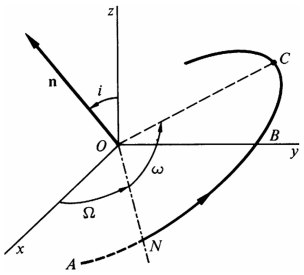

Figure 1: **Schematic of the classical orbital elements**. The vector **n** is normal to the orbital plane, which is offset from the x-y plane by the inclination (ι, denoted here as i). The longitude of the ascending node (Ω) denotes the displacement of the line of nodes (intersecting the orbit at N) from the x-axis, while the argument of periapsis (ω) denotes the angle from N to apoapsis (at C) in the orbital plane. The IMBH is placed at O. This illustration is taken from Goldstein.[2]

torque).

We perform a canonical transformation to switch from position-velocity variables into action-angle variables, which will be more suited to the orbital-type system of interest. We select the classical Delauney variables. They may be expressed in terms of the astronomical elements according to

$$w_1 = \Omega \qquad J_1 = J_2 \cos\iota = L_z \tag{2}$$

$$w_2 = \omega \qquad J_2 = J_3\sqrt{1-e^2} = L \tag{3}$$

$$w_3 = w_3 \qquad J_3 = \sqrt{G m_1 a} \tag{4}$$

L is the total angular momentum of the secondary, while L_z is its projection on the z-axis, and J_3 is the radial action. The central supermassive black hole has mass m_1 and fully determines the Keplerian component of the system's motion. Ω is the longitude of the ascending node, ω is the argument of periapsis, and w_3 is the mean anomaly of the orbit.[2] Fig. 1 illustrates several of the angles. The unperturbed frequencies in these variables are given by $\mathrm{d}w_i/\mathrm{d}t = \Omega_i$, for i ranging from 1 to 3.

The torque τ_z on the perturber can be identified by examining the evolution of the ϕ component of the orbital motion of the secondary, where we use the standard definition of spherical coordinates (r, θ, ϕ).

$$\begin{aligned}\tau_z &= \int \mathrm{d}\mathbf{r}\mathrm{d}\mathbf{v}\frac{\partial\Phi_{\rm ext}}{\partial\phi}f(\mathbf{r},\mathbf{v}) \\ &= \int \mathrm{d}\mathbf{w}\mathrm{d}\mathbf{J}\frac{\partial\Phi_{\rm ext}}{\partial w_1}f(\mathbf{w},\mathbf{J})\,,\end{aligned} \tag{5}$$

after switching to the action-angle variables. We note that Equation (5) implies the torque is second order in the perturbation (since $\int \mathrm{d}\phi\partial\Phi_{\rm ext}/\partial\phi = 0$). Similar to the linear case of standard dynamical friction, the secondary induces a perturbation in the distribution, which then acts on the secondary.

Taking the Fourier transform in the w_i angles and assuming the perturbation amasses over a long timescale, we arrive at, after several intermediate steps outlined in Kaur,[5]

$$\begin{aligned}\tau_z = -\sum_{n_1,n_2,n_3} n_1^2\Omega_3 \int \mathrm{d}\mathbf{J}\mathrm{d}\mathbf{w} \\ \times \frac{\mathrm{d}f}{\mathrm{d}E}\pi\delta(\mathbf{n}\cdot\mathbf{\Omega})|\Phi_{\rm ext}|^2\end{aligned} \tag{6}$$

as the expression for the torque, where the n_i indices categorize the Fourier transform in the w_i angles, with $\mathbf{n}\cdot\mathbf{\Omega} = n_1\Omega_1 + n_2\Omega_2 + n_3\Omega_3$.

Next, we specialize Eq. (6) to the perturbing potential of interest, being that of a compact secondary of mass m_2 rotating about the center of mass (the primary) with a Keplerian velocity $\Omega_{\rm K} = \sqrt{G m_1/(r_2)^3} = -\Omega_3$, where r_2 is the binary's orbital separation. Naïvely, we may assume that due to the disparate length scales of the system (i.e. the orbital scales of the secondary perturber or dark matter particle vs the physical size of the perturber), we can approximate the potential as the Newtonian potential of a point mass of mass m_2. However, Weinberg[9] demonstrated that the torque from a perturbing point mass diverges. For this reason, we will instead consider a Plummer potential

with a length scale b, which we take to correspond to the physical size of the secondary. The potential then has the form

$$\Phi(\vec{r}) = -\frac{Gm_2}{\sqrt{r^2 + r_2^2 - 2rr_2\cos\gamma + b^2}}, \quad (7)$$

where γ is the angle between the radius vectors for the secondary and the field point. To make the expression more tractable analytically, we introduce the variables

$$r_\alpha = 1/\sqrt{2}\,[r^2 + r_2^2 + b^2 + \sqrt{(r^2 + r_2^2 + b^2)^2 - 4r^2r_2^2}\,]^{1/2} \quad (8a)$$

$$r_\beta = \frac{rr_2}{r_\alpha} \quad (8b)$$

This restores the expression to the familiar form

$$\Phi(\vec{r}) = -\frac{Gm_2}{\sqrt{r_\alpha^2 + r_\beta^2 - 2r_\alpha r_\beta\cos\gamma}}. \quad (9)$$

Recognizing $r_\alpha \geq r_\beta$ and boosting to the corotating frame, we have

$$\Phi(\vec{r}, t) = \sum_{l=1}^{\infty}\sum_{m=-l}^{l}\Phi_{lm}(r)Y_{lm}(\theta, \phi - \Omega_{\rm K}t) \quad (10)$$

such that

$$\Phi_{lm}(r) = \frac{4\pi Gm_2}{2l+1}\frac{r_\beta^l}{r_\alpha^{l+1}}Y_{lm}^*(\pi/2, 0). \quad (11)$$

For our system, $\mathrm{d}w_2/\mathrm{d}t = 0$, and therefore Ω_2. With this, the resonance condition $\delta(\mathbf{n}\cdot\mathbf{\Omega})$ fixes the semi-major axis value at $a = (n_3/n_1)^{2/3}r_2$. After several more steps, including implementing this resonance condition, Fourier transforming in mean anomaly w, and integrating in phase space, the final expression for the torque becomes

$$\tau_z = \sum_{l=1}^{\infty}\sum_{n_1=1}^{l}\sum_{n_2=-l}^{l}\sum_{n_3=1}^{\infty}\tau_{n_1,n_2,n_3,l}\,, \quad (12a)$$

with the coefficients $\tau_{n_1,n_2,n_3,l}$ given by

$$\begin{aligned}\tau_{n_1,n_2,n_3,l} =& \frac{512\pi^4G^3m_1m_2^2(r_2)^3}{3}\Omega_{\rm K}\frac{n_3}{(2l+1)^3}\left|Y_{ln_1}(\pi/2,0)Y_{ln_2}(\pi/2,0)\right|^2 \\ &\times\int_0^1 \mathrm{d}e\frac{\mathrm{d}f}{\mathrm{d}\mathcal{E}}e\left|\int_0^\pi \mathrm{d}\psi(1-e\cos\psi)\cos(n_2\nu(\psi) - n_3w_3(\psi))\frac{r_\beta^l}{r_\alpha^{l+1}}\right|^2,\end{aligned} \quad (12b)$$

where $\nu(\psi)$ is the true anomaly as a function of the eccentric anomaly.

This torque corresponds to a drag force as $\tau_z = r_2F_{\rm d}$, with

$$F_{\rm d} = -4\pi\left(\frac{Gm_2}{v_2}\right)^2\log\Lambda\rho(v < v_2). \quad (13)$$

By relating the two quantities, we may determine the effective Coulomb logarithm of the system.

3 Computational Methods

The evaluation of Eq. (12a) requires the nested sum of a two-dimensional integral (eccentric anomaly ψ and eccentricity e) over the quadruple of indices $\{n_1, n_2, n_3, l\}$. This formally describes a quadruple infinite sum. In practice, we must truncate the sums in Eq. (12a) for finite values of n_1, n_2, n_3, and l and estimate the error in this cutoff by identifying the asymptotic behavior of the inte-

gral in each of these indices.

We express the position of the secondary in terms of the eccentric anomaly ψ.

$$\begin{aligned} r = r(\psi) &= a(1 - e\cos\psi) \\ &= (n_3/n_1)^{2/3} r_2 (1 - e\cos\psi), \end{aligned} \tag{14}$$

where in the third equality we use the resonance condition described in Sec. 2.

We denote the ψ integral in Eq. (12b) as I:

$$I(e) = \int_0^\pi d\psi P(e,\psi) \exp(-l g(\psi; e)), \tag{15}$$

where we rewrote $r_\beta^l(\psi)/r_\alpha^{l+1}(\psi)$ in an exponential form, with $g(\psi; e) = \log(r_\alpha(\psi)/r_\beta(\psi))$ and $P(e,\psi) = (1 - e\cos\psi)\,(r_\alpha(e,\psi))^{-1}\cos(n_2\nu(e,\psi) - n_3 w_3(e,\psi))$.

It will prove useful to determine where the majority of the contribution comes from in the integral over eccentricity. This will predominantly be driven by where the maximum of $g(\psi; e)$ is. As such, we wish to determine where $g(\psi; e)$ reaches its maximum value, $\psi = \psi_0$, or equivalently where $g'(\psi = \psi_0; e) = 0$, where $g'(\psi; e)$ denotes the derivative of $g(\psi; e)$ with respect to ψ, evaluated at $\psi = \psi_0$. A simple calculation reveals that this occurs when

$$\begin{aligned} r(\psi = \psi_0) &= (n_3/n_1)^{2/3} r_2 (1 - e\cos\psi_0) \\ &= r_2\sqrt{1 + (b_{r_2})^2} \end{aligned} \tag{16}$$

giving

$$\psi_0 = \arccos\left(\frac{e_{\rm crit}}{e}\right), \tag{17}$$

where we defined $b_{r_2} \equiv b/r_2$ and

$$e_{\rm crit} \equiv \left|1 - (n_3/n_1)^{-2/3}\sqrt{1 + (b_{r_2})^2}\right|. \tag{18}$$

That is, for fixed n_3/n_1 and b_{r_2}, there only exists a real-valued ψ_0, and by extension a maximum of $g(\psi; e)$ within the range of integration in ψ, for $e \geq e_{\rm crit}$. With Eq. (17), $g(\psi_0) = \log\left(b_{r_2} + \sqrt{1 + b_{r_2}^2}\right)$.

3.1 Weinberg Approximation

Weinberg[9] notes that the potential term $(r_\beta/r_\alpha)^l$ is sharply peaked near $r = r_2$ in the limit of large l, and expands $r = r_2(1 + \epsilon)$. Taking $\mathcal{O}(b_{r_2}) = \mathcal{O}(\epsilon)$,

$$\frac{r_\beta^l}{r_\alpha^{l+1}} \approx \frac{1}{r_2}\frac{(1+\epsilon)^l}{\left[1 + \left(1 + \sqrt{\epsilon^2 + b_{r_2}^2}\right)\right]^{l+1/2}}, \tag{19}$$

and noting that most of the contribution comes from the region $\epsilon l \leq 1$ they find

$$\frac{r_\beta^l}{r_\alpha^{l+1}} \propto \frac{1}{r_2} e^{-l\sqrt{\epsilon^2 + b_{r_2}^2}}. \tag{20}$$

This approximation predominantly assumes that most of the contribution to the torque comes from particles whose trajectories cross the pertrubers's orbit, and it highlights low-l modes in which the perturbation potential is locally smooth.

Expanding instead around $r = r(\psi_0)$ and defining $\epsilon \equiv (r(\psi) - r(\psi_0))/r_2 = -e(n_3/n_1)^{2/3}(\cos\psi - \cos\psi_0)/b_{r_2}$, we have

$$I_{\rm Wein}(e) = \int_0^\pi {\rm d}\psi P(e,\psi) \exp\left(-l b_{r_2}\sqrt{1+\epsilon^2}\right) \tag{21}$$

where here $P(e,\psi) = (1 - e\cos\psi)\cos(n_2\nu(\psi) - n_3 w_3(\psi))/r_2$. This serves as an alternative expression for the integral over ψ.

3.2 Saddle Point Approximation

Due to the small physical size of the perturber relative to the system (equivalently, the small b_{r_2}), we anticipate needing to go to high l for the sum in Eq. (12a) to converge. As such, we must consider the high-l limit. This regime is challenging to handle properly, since the ψ integral becomes highly peaked around ψ_0, which we anticipate will occur when $l \sim 1/b_{r_2}$. Additionally, for large n_2 and n_3, the function may also be

highly oscillatory within this peak; this feature comes from the $\cos(n_2\nu(\psi) - n_3 w_3(\psi))$ factor within $P(e,\psi)$. Both of these features significantly complicated the analysis, as numerical integration becomes computationally difficult in this regime. For this reason, in this subsection, we explore a method to analytically compute the integral over ψ. In particular, we apply the method of steepest descent, in which the integral becomes a contour integral over the complex plane.

Consider a complex argument of the exponential $g(z) = u(z) + iv(z)$, where u and v are real functions, which are functions of a complex argument z. In this method, we first determine the stationary points $z_{s,i}$ of $g(z)$ (i.e. where both $u(z_{s,i}) = 0 = v(z_{s,i})$). We then seek to smoothly deform the original contour along the real axis into one which passes through at least one of these stationary points $z = z_s$ and on which $v(z)$ is constant. Along this contour $\mathcal{C}$, the function is no longer oscillatory and we may perform Laplace's method of integration on $u(z)$, centered on z_s.

We now construct the argument for the exponential function for this method. Here, we include the factor of $\cos(n_2\nu(\psi) - n_3 w_3(\psi))$ in the argument. To simplify closing the contour when evaluating in the complex ψ plane, in this subsection we evaluate the integral with bounds $-\pi \leq \psi \leq \pi$. The integral is of the form

$$I(e) = \frac{1}{2}\int_{-\pi}^{\pi} d\psi P(e,\psi)\exp(-lg(\psi;e))\,. \tag{22}$$

If we additionally assume that n_2 and n_3 scale with l (and likewise assume that they are large), then we may write:

$$\begin{aligned} g(\psi;e) = &-\log(r_\alpha(\psi)/r_\beta(\psi)) \\ &- i(N(\nu(\psi) - \zeta w_3(\psi))) \end{aligned} \tag{23}$$

for the generalization of Eq. (15), with $P(e,\psi) = (1 - e\cos\psi)(r_\alpha(e,\psi))^{-1}$. Alternatively, we have

$$\begin{aligned} g(\psi;e) = &-b_{r_2}\sqrt{1+\epsilon^2} \\ &- iN(\nu(\psi) - \zeta w_3(\psi))) \end{aligned} \tag{24}$$

for the generalization of the Weinberg form in Equation (21), with $P(e,\psi) = 1 - e\cos\psi$. Here, $Nl = n_2$ and $\zeta n_2 = n_3$, and by extension $0 < N < 1$ and $0 < \zeta$. As such, we can parameterize the n_i indices in terms of one large index l, as a function of one variable ψ.

While the method of steepest descent may be applied to either of the cases considered (that is, either using Equation (23) or (24)), in practice we only apply this method using Equation (24) as the function in the exponential. The added complexity of Equation (23), particularly in the additional branch cuts introduced due to the logarithm and the square root in Eq. (8a), makes determining the appropriate contours for the saddle point method considerably more challenging. Since the Weinberg exponent is simpler, and we are interested in the high-l regime where this approximation is valid, we only consider Equation (24) for this method.

To compute $I(e)$ using the method of steepest descent, we determine a closed loop of curves which includes the original curve on the real axis from $-\pi < \psi < \pi$ and which additionally passes through two saddle points, and from this we compute the integral using Laplace's method centered on each of the saddles.

3.3 Integral over eccentricity

Having overviewed the strategies for approximating the integral over ψ, we turn next to the remaining integral over eccentricity.

In Fig. 2, we plot the integral $I(e)$ given in Eq. (21) with $n_1 = n_2 = 10$, $n_3 = 15$, and $b_{r_s} = 1/3000$. In the left panel, we plot the contribution for $l = 10$, while in the right we use $l = 100$. We notice that $I(e)$ is oscillatory in its argument, and that

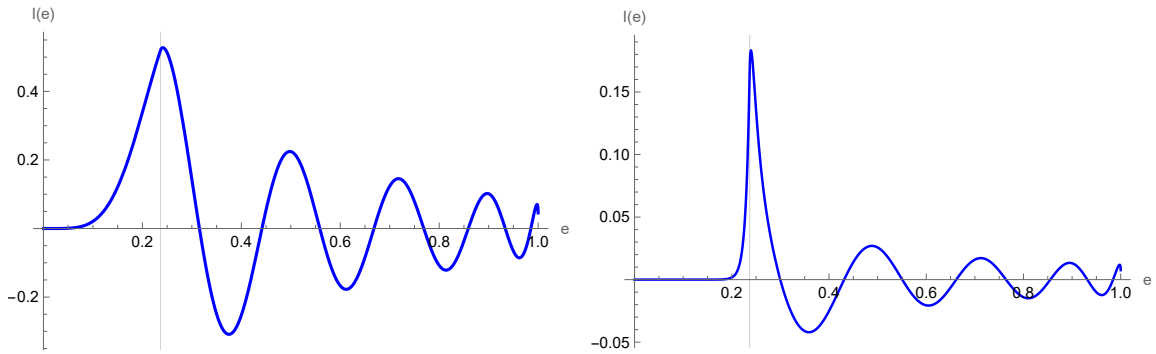

Figure 2: $I(e)$ **for two sets of indices**. Plots of the integral given in Equation (15) for two values of l: $l = 10$ (*left*) and $l = 100$ (*right*). The values of the parameters are $n_1 = n_2 = 10$, $n_3 = 15$, and $b_{r_s} = 1/3000$. We mark $e = e_{\rm crit}$ with a light vertical gray line. More detailed discussion about the figure appears in the text of Sec. 3.3.

it is peaked near $e_{\rm crit}$, particularly as l increases. Furthermore, $I(e)$ falls off quickly for $e < e_{\rm crit}$ in the right panel, which is a general result for large l. As given in Eq. (12b), the lower bound of integration in eccentricity is $e = 0$. However, the above observation suggests that the $0 \leq e < e_{\rm crit}$ region of parameter space is highly suppressed in for large l. Given that the saddle point method is valid in the high l regime, when considering this method we take the lower bound in eccentricity to be $e_{\rm crit}$. When considering the torque when computing the full numerical integral or using the Weinberg approximation, we maintain the lower bound at 0.

On the other hand, we restrict the upper bound in eccentricity in line with the findings by Wade.[8] It was noted there that, for particle trajectories to be stable over an orbital period, they must not plunge into the central black hole. The defining quantity was a critical angular momentum of the particle $J_{\rm min}$. We may relate the orbital angular momentum to the orbital elements as $J = \sqrt{G m_1 a(1-e^2)}$. Thus, a minimum angular momentum in the distribution translates to a maximum allowed eccentricity. Using the resonance condition for the semimajor axis a and using $J_{\rm min} = \sqrt{8} G m_1/c$, we set the upper bound in eccentricity $e_{\rm max}$ to be

$$e_{\rm max} = \sqrt{1 - \frac{8Gm_1}{c^2} \frac{1}{(n_3/n_1)^{2/3} r_2}}. \qquad (25)$$

Hence, for the integration bounds, we use $e \in [0, e_{\rm max}\}$ for the full numerical integral and Weinberg approximation and $e \in [e_{\rm crit}, e_{\rm max}\}$ for the saddle point method.

Functionally, Sec. 3.2 provides a method of analytically computing the ψ integral (that is, it provides an analytical expression for $I(e)$.) When computing the torque directly using Eq. (15) or with (21), we must compute the ψ integral numerically. For all cases, we compute the final integral over eccentricity numerically after computing the ψ integral.

3.4 Conditions on n_i indices

Before moving to compute the torque using the prescription outlined previously, we finish by determining the range of values that the n_i indices may take.

The indices n_1 and n_2 are set according to the spherical harmonic factors in Eq. (12b), in which they run from $-l$ to l. Because of the resonance condition in semimajor axis, we restrict n_1 (as well as n_3) to be positive and nonzero. There is no such condition on n_2, which we take to have either sign and

may be 0. However, n_1 and n_2 must each have the same parity as l for the torque to be nonzero.

Eq. (16) gives the condition for the existence of the extrema ψ_0, meaning that for $(n_3/n_1)^{2/3}\sqrt{1+b_{r_s}} > 2$, there does not exist a real ψ_0. Since the majority of the contribution comes from sets of $\{n_1, n_2, n_3\}$ in which there exists a real ψ_0, we restrict to $(n_3/n_1) < \left(2(1+b_{r_s})^{-1/2}\right)^{3/2}$.

Together, we have the following bounds:

$$n_1 \in \{k \in Z : 1 \leq k \leq l \text{ and } k \equiv l \pmod 2\} \tag{26a}$$

$$n_2 \in \{k \in Z : -l \leq k \leq l \text{ and } k \equiv l \pmod 2\} \tag{26b}$$

$$n_3 \in N = \{1, 2, 3, \ldots\} \tag{26c}$$

with the additional constraints imposed by the condition $(n_3/n_1) < (2/\sqrt{1+b_{r_s}})^{3/2}$.

4 Results

We now turn to evaluating the torque given in Eq. (12a) for a representative system. In this section, we consider a binary with $m_1 = 10^3\,\mathrm{M}_\odot$, $m_2 = 10\,\mathrm{M}_\odot$, and $b = 2Gm_2/c^2$. We place the secondary at $r_2 = 30R_\mathrm{s}$, where $R_\mathrm{s} = 2Gm_1/c^2$, which yields $b_{r_2} = 1/3000$. We consider a distribution function that depends only on specific energy and corresponds to a power law density,

$$\begin{aligned} f(\mathcal{E}) =& \frac{\gamma_\mathrm{sp}(\gamma_\mathrm{sp}-1)}{(2\pi)^{3/2}} \frac{\Gamma(\gamma_\mathrm{sp}-1)}{\Gamma(\gamma_\mathrm{sp}-1/2)} \\ & \times \left(\frac{r_\mathrm{sp}\mathcal{E}}{Gm_1}\right)^{\gamma_\mathrm{sp}} \rho_\mathrm{sp}\mathcal{E}^{-3/2}. \end{aligned} \tag{27}$$

The power law γ_sp falls in the range $[9/4, 5/2]$,[3] and we take $\gamma_\mathrm{sp} = 7/3$ with the normalization $\rho_\mathrm{sp} = 200\,\mathrm{M}_\odot/\mathrm{pc}^3$. The parameter r_sp is given in terms of m_1, γ_sp and ρ_sp[6] as

$$r_\mathrm{sp} \approx \left[\frac{(3-\gamma_\mathrm{sp})0.2^{3-\gamma_\mathrm{sp}} m_1}{2\pi\rho_\mathrm{sp}}\right]^{1/3}. \tag{28}$$

We evaluate the torques using a MATHEMATICA script[4] written by the author.

In Fig. 3, we plot $\tau_{n_1,n_2,n_3,l}$ (given by Eq. (12b)) for different values of l for the four methods described in Sec. 3: numerical integration of the original integral (using $I(e)$ from Eq. (15)) in blue, numerical evaluation of Weinberg's approximation to the exponent (Eq. (21)) in orange, and the saddle point method of evaluating Eq. (21) (as described in Sec. 3.2) in gray. In the left panel, we use the triplet $\{n_1, n_2, n_3\} = \{1, 1, 1\}$, while in the right we use $\{n_1, n_2, n_3\} = \{2400, -3000, 3250\}$. We examine the former before moving to the latter.

For the case of $n_1 = n_2 = n_3 = 1$, we observe that the full numerical and Weinberg results (blue and orange lines, respectively) agree well for small l, though they disagree for large l ($l > 10^3$). This is because the evaluation of the full integral becomes inaccurate, as the integrand in Eq. (15) becomes increasingly sharply peaked and this peak is missed by numerical integration. At large l ($l > 3 \times 10^3$), we observe that the saddle point method results approach those with the Weinberg approximation.

For the case of $n_1 = 2400$, $n_2 = -3000$, $n_3 = 3250$, we begin at larger value of l (given that $n_2 = -3000$ requires $l \geq 3 \times 10^3$). The Weinberg and saddle point methods agree well through the entirety of the range, ranging from a $\sim 10\%$ difference at $l = 3 \times 10^3$ to a $\sim$ few% difference at $l = 10^5$. When directly integrating without any approximations, the result is everywhere underestimated (though, again, it can be shown to agree with the Weinberg result by enforcing a sufficiently large internal precision when numerically integrating.)

We return to the left panel of Fig. 3. Closer examination for small l suggests that the full numerical integral and Weinberg methods do not agree well for the smallest values of l, but do at slightly larger values.

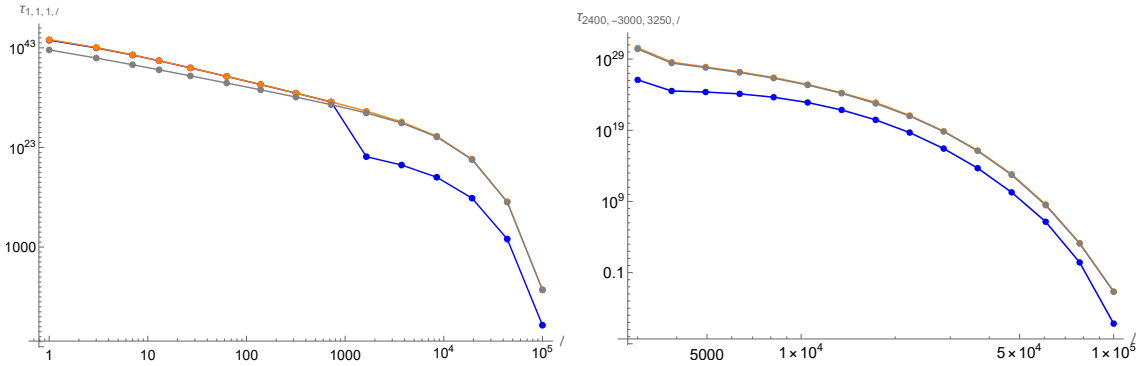

Figure 3: **Torque values as a function of l for two triplets of $\{n_1, n_2, n_3\}$ with different computational methods**. Values of $\tau_{n_1,n_2,n_3,l}$ (Eq. (12b)) as a function of l for two representative triplets of the n indices: *left*: $n_1 = n_2 = n_3 = 1$, and *left*: $n_1 = 2400$, $n_2 = -3000$, $n_3 = 3250$, given in CGS units. Each color corresponds to a different computational strategy. $\tau_{n_1,n_2,n_3,l}$ is evaluated at 15 points for a given method, which are denoted by dots and are connected by intermediate lines. The blue line is the torque computed using the full numerical integral, while the orange is that using the Weinberg approximation. The gray line corresponds to the saddle point method of integration. More detailed discussion about the figure appears in the text of Sec. 4.

This reflects the fact that the Weinberg approximation is based on an expansion of the contribution around $r(\psi_0)$, and is therefore most accurate when the majority of the integrand of $I(e)$ is localized around $\psi = \psi_0$. This becomes a better assumption as l increases, and is not well satisfied for the lowest l values. For this reason, we expect the Weinberg method to accurately approximate the full integral as l increases. Indeed, by increasing the resolution of the numerical integrator within MATHEMATICA (namely, increasing the internal precision at which it carries out its calculations), we find that the results for the full numerical integral and the Weinberg approximation can be shown to agree for large l, implying the Weinberg approximation accurately captures the torque for this triplet of n_i indices. However, evaluating the full integral with this precision is considerably less efficient and takes significantly more time to evaluate. For this reason, we use the Weinberg result where it is valid, as opposed to the full integrand.

The ultimate goal is to identify a scheme for evaluating the torque across values of the l and n_i indices. As seen in Eq. (12a), we must sum over the three n_i indices as well as l. Fig. 3 suggests that the torque smoothly changes (for fixed $\{n_1, n_2, n_3\}$) as l is increased. Therefore, for fixed $\{n_1, n_2, n_3\}$, we may evaluate the torque for different values of l, selecting the appropriate method for integrating the integral over ψ. The above discussion suggests that the full numerical integral may be used at the lowest values of l until it sees a sufficient level of agreement (a $\sim$ few% level) with the Weinberg approximation, or at most $l \sim 1/b_{r_s}$. The Weinberg approximation will be valid to high l, but becomes computationally expensive as l increases and may become inaccurate to evaluate numerically, since the integrand in Eq. (15) becomes very sharply peaked in this regime. Therefore, we recommend switching to an analytic expression for $I(e)$ for these values of l. Fig. 3 suggests that saddle point method is a good approximation in this limits. This scheme will work across l and can be used for when evaluating over other values of the n_i indices.

5 Conclusions

In this chapter, we discussed an application of resonant torque theory to the inspiral of compact objects. We noted that classical dynamical friction may fail for spherical systems, and introduced spherical torque theory as an alternative. We then constructed the expression for spherical torques, and specialized this expression to the compact-binary system of interest, reducing it to quadruple sum of two-dimensional integrals. Given the numerical challenges posed by having a compact object source the perturbations (namely, contributing to difficulties related to convergence of the sum over Fourier modes), we explored computational methods to facilitate faster evaluation of the relevant integrals across multipole orders, labeled by l. In doing so, we identified regions of l which are well captured by different integration strategies, which can then be used when summing up the terms to compute the final torque at a given orbital separation.

A natural next direction for this work is in finalizing the sum over the n_i and l indices, as suggested by Eq. (12a). Given the semi-infinite sum over four indices, careful consideration about the asymptotics of the sum should be taken. This will give the final value for the torque, which may be compared against the Chandrasekhar expression to calibrate the Coulomb logarithm.

References

[1] S. Chandrasekhar. Dynamical Friction. I. General Considerations: the Coefficient of Dynamical Friction. *The Astrophysical Journal*, 97:255, mar 1943.

[2] Herbert Goldstein, Charles Poole, and John Safko. *Classical Mechanics (3rd Edition)*. 06 2001.

[3] Paolo Gondolo and Joseph Silk. Dark matter annihilation at the galactic center. *Phys. Rev. Lett.*, 83:1719–1722, 1999.

[4] Wolfram Research, Inc. Mathematica, Version 14.2. Champaign, IL, 2024.

[5] Karamveer Kaur and S. Sridhar. Stalling of globular cluster orbits in dwarf galaxies. *The Astrophysical Journal*, 868(2):134, December 2018.

[6] Bradley J. Kavanagh, David A. Nichols, Gianfranco Bertone, and Daniele Gaggero. Detecting dark matter around black holes with gravitational waves: Effects of dark-matter dynamics on the gravitational waveform. *Phys. Rev. D*, 102(8):083006, 2020.

[7] Scott Tremaine and Martin D. Weinberg. Dynamical friction in spherical systems. *Monthly Notices of the Royal Astronomical Society*, 209(4):729–757, 08 1984.

[8] Benjamin A. Wade and David A. Nichols. Intermediate mass-ratio inspirals in a dense dark-matter environment: Effects of the initial dark-matter distribution. *Phys. Rev. D*, 113(4):044014, 2026.

[9] Martin Weinberg. Orbital decay of satellite galaxies in spherical systems. *The Astrophysical Journal*, 300:93–111, 12 1985.